Title

Direct observation of the local microenvironment in inhomogeneous CO 2 reduction gas diffusion electrodes via versatile pOH imaging

Journal

Energy & Environmental Science, 16(4)

ISSN

1754-5692

Authors

Böhme, Annette

Bui, Justin C

Fenwick, Aidan Q

et al.

Publication Date

2023-04-12

DOI

10.1039/d2ee02607d

Direct Observation of the Local Microenvironment in Inhomogeneous CO_2 Reduction Gas Diffusion Electrodes via Versatile pOH Imaging

Author Names

Annette Boehme[1,2], Justin C. Bui[3,4], Aidan Fenwick[2,5], Rohit Bhide[6], Cassidy N. Feltenberger[6,7], Alexandra J. Welch[1,2], Alex J. King[3,4], Alexis T. Bell[3,4], Adam Z. Weber[4], Shane Ardo[6,7,8,9], and Harry A. Atwater*[1,2]

Author Information

[1]Department of Applied Physics and Material Science,
California Institute of Technology,
Pasadena, CA 91125, USA

[2]Liquid Sunlight Alliance,
California Institute of Technology,
Pasadena, CA 91125, USA

[3]Department of Chemical and Biomolecular Engineering,
University of California Berkeley,
Berkeley, CA 94730, USA

[4]Liquid Sunlight Alliance,
Lawrence Berkeley National Laboratory,
Berkeley, CA 94730, USA

[5]Department of Chemistry and Chemical Engineering,
California Institute of Technology,
Pasadena, CA 91125, USA

[6]Department of Chemistry,
University of California Irvine,
Irvine, CA 92697, USA

[7]Liquid Sunlight Alliance,
University of California Irvine,
Irvine, CA 92697, USA

[8]Department of Chemical and Bimolecular Engineering,

University of California Irvine,

Irvine, CA 92697, USA

[9]Department of Materials Science and Engineering,

University of California Irvine,

Irvine, CA 92697, USA

Corresponding Author:

*E-mail: haa@caltech.edu

Abstract

We report how the micrometer-scale morphology of a carbon dioxide reduction (CO_2R) gas diffusion electrode (GDE) affects the mass transport properties and with it, the local CO_2R performance. We developed a technique to probe the microenvironment in a CO_2R GDE via local pOH imaging with time- and three-dimensional spatial micrometer-scale resolution. The local activity of hydroxide anions (OH^-), represented by the pOH value, around a GDE in contact with an aqueous electrolyte is a crucial parameter that governs the catalytic activity and CO_2R selectivity. Here, we use fluorescence confocal laser scanning microscopy (CLSM) to create maps of the local pOH around a copper GDE by combining two ratiometric fluorescent dyes, one of which is demonstrated as a pOH sensor for the first time in this work. We observe that the local pOH decreases when current is applied due to the creation of OH^- as a byproduct of CO_2R. Interestingly, the pOH is lower inside microtrenches compared to the electrode surface and decreases further as trenches become narrower due to enhanced trapping of OH^-. We support our experimental results with multiphysics simulations that correlate exceptionally well with measurements. These simulations additionally suggest that the decreased pOH inside microcavities in the surface of a CO_2R GDE leads to locally enhanced selectivity towards multicarbon (C_{2+}) products. This study suggests that narrow microstructures on the length scale of 5 µm in a GDE surface serve as local CO_2R hotspots and highlights the importance of a GDE's micromorphology on the CO_2R performance.

Introduction

It is crucial to store renewable energy effectively for long time periods in order to reach the negative CO_2 emissions required to mitigate the consequences of climate change. Accordingly, the concept of electrochemical CO_2 reduction (CO_2R) is compelling because it enables the storage of renewable energy in the form of chemical bonds. CO_2R establishes CO_2 and water (H_2O) as the primary sustainable feedstocks to form useful chemicals and fuels, thereby closing the carbon cycle.[1-(4)]

Though there have been many encouraging advances in the field of electrochemical CO_2R, the process is highly complex and there are still challenges that must be overcome before this technology is energy-efficient and selective enough to be used at an industrial scale.[1,(3),(5)] One promising approach is the use of gas diffusion electrodes (GDEs).[(6)-(8)] This type of electrode addresses the problem of mass transfer limitations that are encountered in conventional catalytic setups by delivering CO_2 in the gas phase to a catalyst in contact with a liquid electrolyte. Most GDEs consist of a macroporous gas diffusion

layer topped with a hydrophobic microporous layer that is then subsequently coated with a catalyst.[9]-[11] (**Figure 1c**). In many cases, the catalyst is wetted by a thin layer of aqueous electrolyte to provide ionic conductivity but not limit CO_2 transport to the surface.[10],[12] This setup allows for increased current densities by more than one order of magnitude over conventional setups: For a conventional setup in which two electrodes are placed in CO_2-saturated electrolyte, mass transport to the cathode limits the rate of CO_2 consumption and hence, the maximum current density magnitude does not exceed 30 mA/cm^2. On the other hand, tailored GDEs with current density magnitudes larger than 1 A/cm^2 have been demonstrated.[13],[14]

Various parameters influence the activity and selectivity of a GDE, and it is the interplay between these operating parameters that dictates the CO_2R performance. It is therefore important to understand the impact of each parameter. One very important parameter that influences the system's performance is the choice of catalyst material.[15]-[17] The most commonly studied CO_2R catalyst is copper, because its moderate binding energy to CO as a reaction intermediate allows for its further reduction to desirable higher-order carbon products such as ethanol, propanol, ethylene, and acetate.[16],[18],[19] Furthermore, in determining the selectivity and activity of CO_2R, the composition and structure of the GDE, i.e. pore size, hydrophobicity, surface depositions or the presence of microstructures, play an ill-understood role.[9],[10],[20],[21] Other parameters include the applied potential, the properties of the electrolyte (e.g. the constituent ions and the viscosity), the cell configuration, and the choice of ion-exchange membranes.[13],[18],[19],[22]-[24] In addition to these, the local activities of hydroxides, a_{OH^-}, and protons, a_{H^+}, for which the pOH and pH values are a measure, are critical because both species are involved in the CO_2R process[19],[25], as per equations S19-S26. The pOH value is defined as $pOH = -log_{10}(a_{OH^-})$ and the pH value as $pH = -log_{10}(a_{H^+})$. In many cases, hydroxide and proton activity can be approximated as the concentration. At equilibrium, $pH + pOH = pK_w$, with pK_w = 14 under ambient conditions, so if the system is in equilibrium, the pH can be directly inferred from the pOH.[26]

For a GDE at open circuit, CO_2 diffuses through the macroporous and microporous layers into the electrolyte where it rapidly reacts with OH^- to form bicarbonate and carbonate anions, according to the chemical equilibrium reactions listed in equations S8 – S12.[27]-[29] This decreases the local OH^- concentration and thereby increases the pOH in the electrolyte. This process is schematically depicted in **Figure1c** (left side). Due to the participation of CO_2 in these buffer reactions, the ability to map the spatially and time-resolved pOH around a GDE enables us to assess the local concentration of CO_2 in the electrolyte around a GDE.

At a non-zero current, a portion of the CO_2 molecules is reduced to form products such as carbon monoxide, formic acid, methane or ethylene, among others[11],[18],[19],[30]-[32], as per equations S19 – S26. During this non-equilibrium process, one OH^- is created, or one buffer species is deprotenated for each electron involved.[33] The same holds true for the competing hydrogen evolution reaction (HER) that must be suppressed to maximize the CO_2R yield. As a result, at sufficiently high current densities, we expect that the pOH will decrease, as is depicted schematically in **Figure1c** (right side). This effect is in competition with an increase in pOH caused by unreduced CO_2 molecules that undergo reactions to form bicarbonate and carbonate anions. As a result, a low observed pOH indicates the presence of CO_2 reduction activity.

In addition, it has been shown that the pH and pOH themselves have a substantial impact on the reactivity and selectivity of CO_2R. It has been demonstrated that high pH (corresponding to low pOH) suppresses the parasitic HER[25],[34] and shifts the CO_2R selectivity towards C_{2+} products.[8],[25],[32],[35] The

reason for the latter is that OH^- actively suppresses the creation of single carbon products (C_1) and hydrogen molecules (H_2), while it does not affect the C_{2+} current density. This leads to an increased Faradaic efficiency (FE) towards C_{2+} products at a given current density[35],[36].

As a result, knowledge of the pOH in the vicinity of an operating GDE is critical and can aid researchers in better optimizing the performance of a GDE. Notably, the pOH is expected to vary as a function of distance from the electrode surface. In addition, it also varies in the plane parallel to the surface if there are any inhomogeneities such as microcavities present on the surface. For these reasons, a measuring technique that allows one to map to pOH around an operating GDE with high resolution in three dimensions is desired.

Previous efforts towards this end have included theoretical studies of the pH around GDEs performing CO_2R.[10],[37],[38] Experimental approaches have involved scanning electrochemical microscopy (SECM)[39],[40], surface-enhanced Raman (SERS)[41], electrochemical atomic force microscopy (EC-AFM)[42] and surface-enhanced infrared spectroscopy (SEIRAS).[34] While all these techniques are powerful and can reach spatial resolutions on the nanometer scale, they do not have the ability to map the operando pH/ pOH of an entire macroscopic sample in three spatial dimensions. Fluorescent confocal laser scanning microscopy (CLSM), a well-known technique in the context of electrochemistry,[43]-[48] is our method of choice to address these concerns in the context of CO_2R because it enables time-resolved measurements in three spatial dimensions. The spatial resolution of this technique can reach 250 nm under ideal conditions. The time resolution is, depending on the size and spatial resolution of the frame of interest, microseconds to several seconds. The combination of time resolution with sub-micrometer spatial resolution in three spatial dimensions with high accuracy is what makes this pOH-mapping technique unique. Importantly, it enables the map the local pOH value under operating conditions over a wide current density scale, from 0 to at least 200 mA/cm^2 in magnitude. To map the operando pOH in three dimensions with high resolution is important because it allows us to probe the pOH within microstructures on the surface of a sample of interest such as an active GDE. No other technique allows to probe the operando pOH within cavities in the surface of a GDE. This capability presents the unique opportunity to correlate the microstructure geometry of a GDE with its CO_2R performance. Understanding the local chemical microenvironment near a CO_2R catalysts is key for understanding selectivity and performance of these devices, as well as to validate continuum level theories of CO_2R in porous electrodes.[58] Furthermore, our novel technique might also prove to be useful for the investigation of other electrochemical applications beyond CO_2R.

In previous experiments,[49] we used the commercially available ratiometric fluorescent photoacid dye 6,8-dihydroxypyrene-1,3-disulfonic acid disodium salt (DHPDS), which is sensitive to pH values between 6 and 10. The term 'ratiometric fluorescent dye' refers to a probe with a spectrum that exhibits at least two distinct peaks with intensities changing in opposite directions upon varying the parameter to which the probe is sensitive. By evaluating the ratio between the peak intensities, the observed signal becomes independent of the local dye concentration.[50]-[52] The sensing mechanism of the photoacid DHPDS involves proton-transfer reactions in its electronic ground state to perturb its absorption spectrum. This is the mechanism used by nearly all fluorescent pH indicators in biological studies at near-neutral-pH conditions.[53] With DHPDS, we observed that the local pH at the GDE surface increased from pH 6.8 to greater than 10 as the magnitude of the current density was increased from 0 to -28 mA/cm^2 in 100 mM $KHCO_3$ electrolyte. We showed that the pH increased locally inside trenches 5 – 20 µm wide in the GDE surface. Furthermore, the pH increased as the trench width diminished which indicated that narrow trenches exhibit higher CO_2R activity than wider trenches and planar surfaces.[49] While these results were insightful, they were limited by the pH range in which DHPDS is sensitive. We observed that

the DHPDS signal saturated at current density magnitudes larger than -20 mA/cm^2 in 100 mM $KHCO_3$. However, there is an interest in operating GDEs at high current densities to increase the CO_2R rate up to industrially relevant-levels (|J|>100 mA/cm^2).[54],[55] Therefore, for this study, we developed a new sensing protocol based on our recent discovery of an excited-state proton-transfer mechanism for weak photoacids, such as 8-aminopyrene-1,3,6-trisulfonic acid trisodium salt (APTS). Unlike DHPDS, at near-neutral-pH and alkaline-pH conditions APTS does not undergo proton-transfer reactions in its electronic ground state. Instead, the fluorescent signal of APTS is altered via quenching of its thermally equilibrated electronic excited state by direct proton transfer to aqueous OH^-.[56] We also show herein that aqueous dissolved inorganic carbon species do not interfere with this process (**Figure S1**). Owing to our newly characterized mechanism, the aromatic amine form of APTS can be used as a probe for the pOH value and is sensitive to pOH values between 0 and 2.8, compared to pOH 4 - 8 for DHPDS. It must be emphasized that this is the first demonstration of APTS as a sensor for the local pOH. APTS exhibits a novel sensing mechanism and greatly enhances the capabilities of our technique to map the local pOH value with CLSM. By combining DHPDS with APTS, we are now able to cover a pOH range from 0 to 8 (with a gap between 2.8 and 4) and investigate operating GDEs under current densities as large in magnitude as -200 mA/cm^2. Additionally, we explore the influence of different bicarbonate concentrations in the electrolyte and of different microstructure geometries. All told, the work crucially enables a correlation between the bulk electrolyte properties and electrode structure with the pH present at the electrochemical active site across a broad range of operating current densities. We also evaluate the CO_2R performance of our GDEs with gas chromatography measurements and supplement our experimental analysis with continuum modeling to enables a better understanding of the correlation between local pH and CO_2R performance.

Experimental

CLSM with the two fluorescent dyes DHPDS and APTS was used to map the pOH around an operating GDE performing CO_2R over a wide pOH range. An electrochemical cell compatible with CLSM was developed, depicted schematically in **Figure 1a** as a cross section and **Figure 1b** as a top view. The electrochemical cell comprises of an electrolyte chamber with two perpendicular electrolyte inlets and outlets and is open at the top which allows the water immersion objective of the confocal microscope to be immersed into the electrolyte. For experiments at constant current densities, a leakless silver/silver chloride reference electrode and a platinum mesh counter electrode are submerged into the electrolyte. This cell enables us to study a GDE that is fed with gaseous CO_2 through a gas chamber. The GDE is made of a Sigracet 22 BB carbon paper substrate covered with 300 nm Cu as well as a carbon black, graphite and Nafion coating. The substrate's surface is covered by an irregular pattern of trenches 5 – 30 µm wide which is shown schematically as a cross section in **Figure 1c** as well as in a top-down scanning electron microscopy (SEM) image in **Figure 1d**. The trenches cover approximately 6% of the sample surface. Energy dispersive X-ray spectroscopy (EDS) measurements reveal that copper covers not only the planar carbon paper surface but also the trench walls and bottoms (**Figure S2**). The maximum spatial resolution of the confocal microscope is 250 nm in the x-y plane and 500 nm in the z-direction, however, electrolyte flow introduces noise, so the resolution is estimated to be on the order of one micron. We investigate features that are no smaller than 5 µm, so this resolution is satisfactory.

We first used the dye APTS in the absence of electrical current to investigate the diffusion of CO_2 through a GDE. For this, 1 M KOH electrolyte (pOH 0) with 100 µM APTS was used. The fluorescence signal was mapped in the plane perpendicular to the electrode surface as a function of time with one frame captured approximately every four seconds. After one minute of continuous measurements, a 10 standard

cubic centimeters per minute (SCCM) CO_2 gas stream was fed into the gas chamber of the electrochemical cell and the change in pOH in the electrolyte was observed. The measurements were performed both with and without circulating the electrolyte at a rate of 6 mL/min.

In addition, we used both dyes, DHPDS and APTS, to map the pOH around an operating GDE performing CO_2R at current densities between 0 mA/cm^2 and -200 mA/cm^2. Measurements were performed in the plane parallel to the electrode surface, at 20 µm above the surface, at the surface, and at 20 µm below the surface inside a trench. A CO_2-saturated aqueous $KHCO_3$ solution with $KHCO_3$ at concentrations of 100 mM, 200 mM and 400 mM spiked with 100 µM DHPDS or 200 µM APTS was used as the electrolyte and pumped through two perpendicular inlets at a rate of 6 mL/min. The CO_2 gas flow through the gas chamber was set to 10 SCCM. The electrolyte with dilute dye was removed from the cell and replaced after each measurement. Every measurement was performed at least three times.

We further evaluated the CO_2R performance of equivalent copper on carbon paper GDEs with gas chromatography. We used an electrochemical cell that was tailored for use with gas chromatography. More details about the sample fabrication and characterization, dye calibration, and measuring procedure can be found in the Supporting Information, section **S1** and **Figures S2 – S4**.

The development of the multiphysics model, including the physics, parameters, and assumptions employed, is described in the Supporting Information, section **S2** and **Figure S11**.

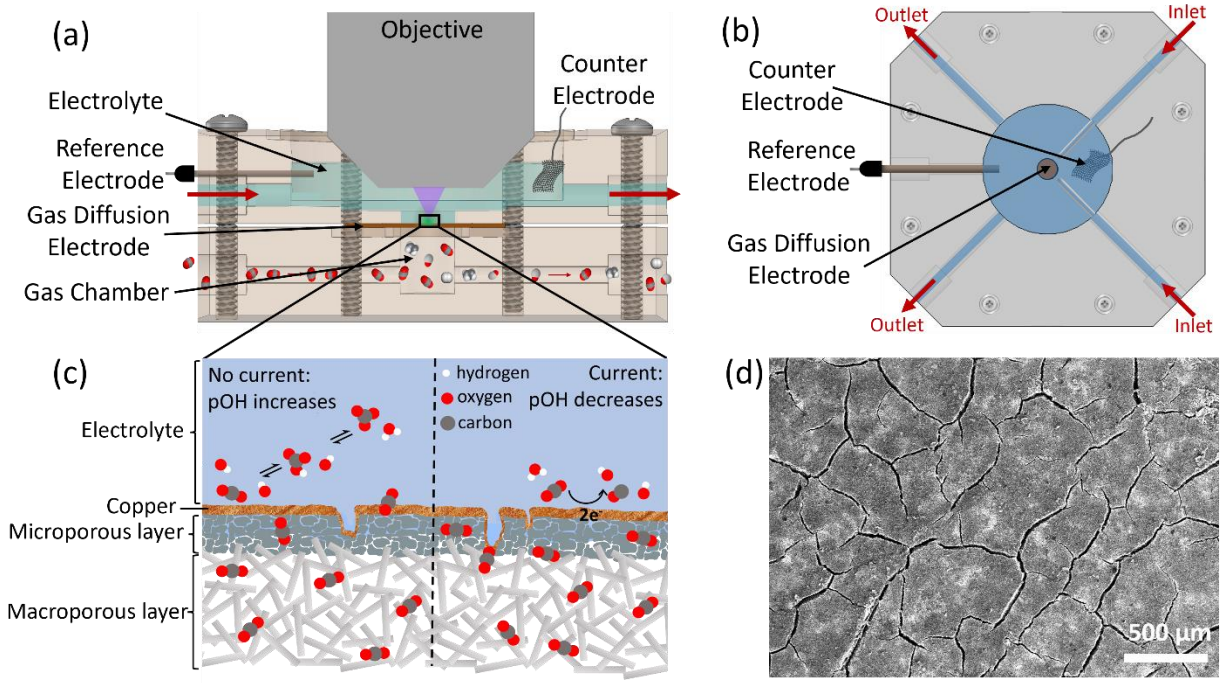

***Figure 1**: **(a)** Cross section of the electrochemical cell with water-immersion objective. The reference electrode is a leakless Ag/AgCl electrode, the counter electrode is a Pt mesh. **(b)** Top view of the electrochemical cell showing two perpendicular electrolyte inlets and outlets. **(c)** Schematic cross section of the carbon paper GDE (not to scale), the left hand side depicts the pOH increase if no current is passing, the right hand side shows the pOH decrease with applied current. **(d)** Top-down SEM image of the GDE surface (Sigracet 22BB carbon paper with 300 nm Cu).*

Results and Discussion

First, we investigated how the local pOH in the electrolyte surrounding a GDE changed upon exposure to CO_2 at open circuit. This allowed us to draw conclusions about the diffusion of CO_2 molecules through a GDE. Our developed measuring technique is ideal for this study as it combines time resolution with the capability to spatially resolve the local pOH inside inhomogeneities in the surface of a GDE. CO_2 reacts with OH^- and water molecules in the electrolyte to form bicarbonate and carbonate anions. This increases the pOH which becomes an indicator for the CO_2 diffusion pattern. **Figure 2a** shows color-coded maps of the local pOH in the plane perpendicular to the electrode surface as a cross-section through a trench as well as the above electrolyte for different times without electrolyte flow. We define t = 0 s as the time when the CO_2 flow through the gas chamber of the electrochemical cell was turned on. A distinct change in pOH is immediately visible in the first frame after starting the CO_2 flow but it is restricted to the trench. The pOH changes at the electrode surface and in the bulk electrolyte as time proceeds. In **Figure 2c**, the average pOH at three different positions is tracked as a function of time. To this end, we draw a line 20 µm above the electrode surface (+20 µm), at the electrode surface (0 µm), and 20 µm below the electrode surface inside the trench (-20 µm) as indicated in the first panel of **Figure 2a**. The pOH is averaged along these lines as a function of time. The vertical gray line in **Figure 2c** indicates the time when the CO_2 gas supply was turned on. This data confirms that the pOH first changes inside the trench, then at the GDE surface and approximately five seconds later at 20 µm above the surface, which is consistent with the gaseous CO_2 feed coming from the backside of the GDE. After 20 s, the pOH values converge at all positions monitored and remain constant for the duration of the experiment. An analogous measurement was performed in a region of the electrode void of trenches (**Figure S5**) and we observed that the pOH increases at a slower rate in comparison to measurements at a location with a trench. This demonstrates that microstructures such as trenches promote faster CO_2 transport through a GDE substrate.

The experiment displayed in **Figure 2a** was repeated under an electrolyte flowrate of 6 mL/min (**Figure 2b**). This has a dramatic effect on the pOH around the GDE: The first change in pOH is only visible after 19 s, compared to less than 5 s without electrolyte flow. A significant increase in pOH caused by the diffusion of CO_2 is solely observed inside the trench. **Figure 2d** tracks the pOH over time in a similar manner as **Figure 2c**. This confirms that the pOH increases little at the GDE surface as well as 20 µm above the surface, and even within the trench, the pOH remains below the value obtained without electrolyte flow. A steady state, with constant pOH up to 20 µm above the electrode surface, is reached after 40 s. However, the pOH at the three locations never converges to a single value, in contrast to the measurements performed with stationary electrolyte. Electrolyte flow results in a well-defined boundary layer around the GDE surface which leads to a CO_2 concentration gradient. The boundary layer is taken into consideration in the multiphysics model. In the absence of electrolyte recirculation, diffusion is the dominant transport mechanism for CO_2 and subsequent CO_2R products. When the electrolyte is circulated however, convection dominates the mass transfer and causes OH^- to be more quickly removed from the GDE surface. This prevents the pOH from rising as much as it would without electrolyte flow. As the electrolyte is more stationary inside trenches, a larger pOH increase can be observed in these confined spaces.

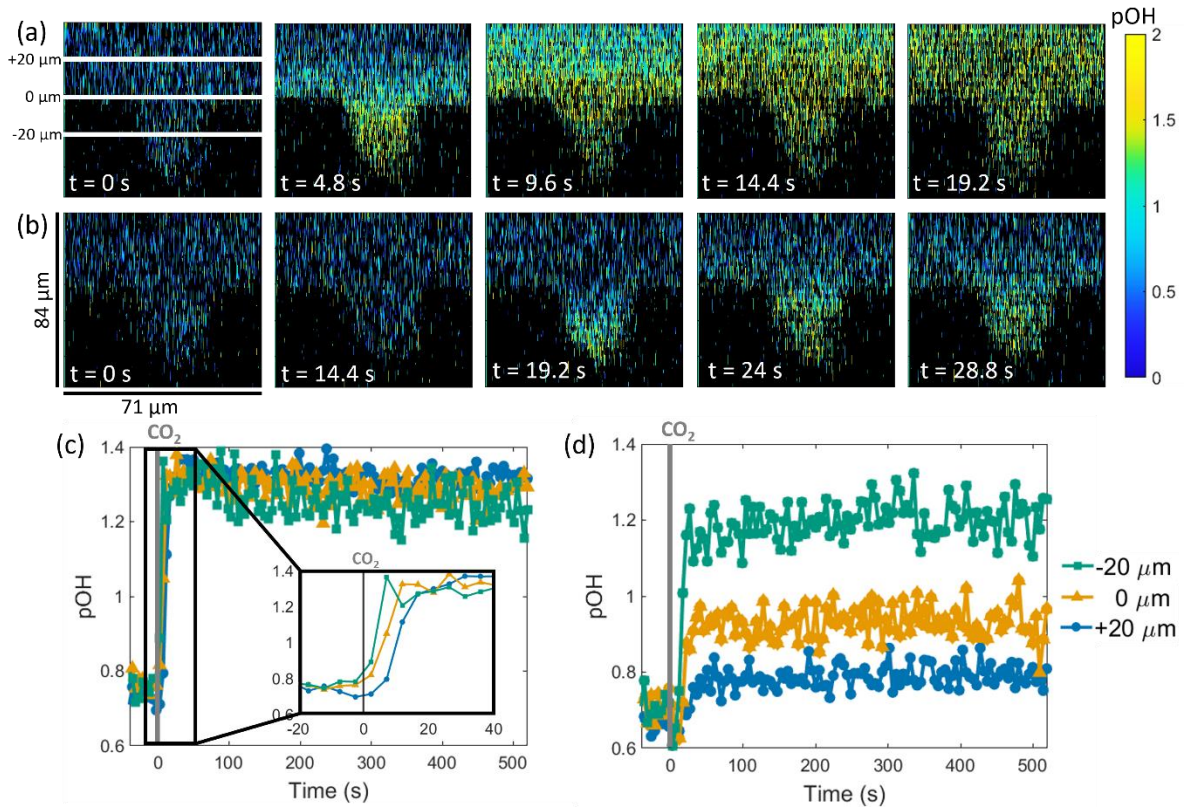

Figure 2: *Changing pOH in the electrolyte due to CO_2 diffusion around a trench in a carbon paper GDE at open circuit, without electrolyte flow **(a, c)** and with electrolyte flow **(b, d)**. Measurements performed with 1M KOH electrolyte with 100 µM APTS, 10 SCCM CO_2 turned on at the backside of the electrode at t = 0 s. Frames in **(a)** and **(b)** show pOH maps as a cross section through a trench in the plane perpendicular to the electrode surface for different times. The scale bars apply to both **(a)** and **(b)**.* Panels ***(c)*** *and* ***(d)*** *track the average pOH at locations 20 µm above the surface (+20 µm), at the surface (0 µm) and 20 µm below the surface in the trench (-20 µm), as specified in the first frame of **(a)**, as a function of time. The vertical gray lines indicate the start of the CO_2 flow.*

An additional study was conducted to compare the CO_2 diffusion through homogeneous GDE substrates made of laminated polytetrafluoroethylene (PTFE) with pore sizes that are specified by the manufacturer as 0.1 to 0.2 µm and 0.45 µm, respectively. **Figure S6** shows a schematic representation of the structure of both a carbon paper GDE and a PTFE GDE together with SEM images. **Figure S7** compares the flow patterns through PTFE GDEs with different pore sizes. We observe that, as expected, the pOH in the electrolyte above the surface increases faster for PTFE with a larger pore size. After 45 seconds it converges to the same value for both substrates. This result gives evidence that, not only microcavities in a GDE's surface, but also larger pore size can promote faster CO_2 transport. However, there is a critical pore size that should not be exceeded, otherwise the pores will be flooded with liquid electrolyte during an experiment. We observed this for a laminated PTFE substrate with pore sizes of 5 µm or greater. Flooding prevents effective CO_2 transport and inhibits CO_2 diffusion to catalytic sites.[10],[12] These results suggest that consideration of the influence of microstructures, even in commercially available GDE substrates, is a critical parameter to understand device performance.

The focus of our study is to investigate the local pOH around an operating GDE performing CO_2R over a wide range of current densities. Our newly developed technique allows to perform pOH measurements with superior three-dimensional resolution inside cavities in an electrode under operating conditions. To ensure that our GDE samples (300 nm Cu on carbon paper) perform CO_2R, we evaluated their CO_2R performance with gas chromatography. We performed chronopotentiometry experiments for different current densities. Our results are consistent with copper GDEs previously reported in literature[15],[18],[57]. H_2 production dominates for low current density magnitudes. As the magnitude of the current density increases, we observe more CO_2R products, and the selectivity shifts towards C_{2+} products. We observe ethylene for current densities of -50 mA/cm^2 or higher in magnitude and ethanol for -200 mA/cm^2 (**Figure S8**). We can therefore assume that the analogous electrodes we use for our pOH imaging experiments behave as one would expect from literature.

By combining the two pOH-dependent fluorescent ratiometric dyes, DHPDS and APTS, we are able to cover the pOH range from 0 to 8. In the context of CO_2R, a low local pOH under operation indicates high CO_2R activity and is desirable because it has been shown that high pH can help suppress the parasitic HER and favor the formation of C_{2+} products.[8],[25],[32],[35],[36] **Figure 3** displays pOH maps in the plane parallel to the electrode surface in 100 mM $KHCO_3$ electrolyte for different current densities between 0 mA/cm^2 and -100 mA/cm^2 and at three different z-positions: 20 µm above the electrode surface, at the electrode surface, and 20 µm below the electrode surface inside a trench. The panels on the left-hand side were captured using DHPDS, and the ones on the right-hand side were captured using APTS.

We observed that APTS degrades and slowly loses its fluorescence for high current densities. We hypothesize that this is connected to the reduction of APTS at the electrode surface. A more detailed analysis of this effect can be found in the Supporting Information, section S1. Despite the slow degradation of APTS, the pOH measurements obtained with APTS are reliable because APTS is a ratiometric dye. The pOH value is calculated from the ratio between two signals that are captured independently in two different wavelength intervals. As some dye molecules degrade, both signals become weaker. This leads to a decreased signal-to-noise ratio, however, the ratio between both signals remains unchanged (see **Figure S9**). The dye degradation effect could be mitigated by using an APTS concentration of 200 µM (compared to DHPDS, where 100 µM is sufficient), removal and replacement of the electrolyte after each measurement, and the introduction of two perpendicular electrolyte inlets to ensure the transportation of fresh APTS to the GDE surface. Some of the panels under high current densities still appear relatively dark and noisy. This is especially evident inside the trench as the electrolyte is more stationary in confined spaces and this encumbers the transport of fresh, undegraded dye. However, since APTS is a ratiometric dye, the pOH it predicts does not depend on concentration. At magnitudes of the current density as high as -200 mA/cm^2, we were still able to collect enough fluorescence signal to determine the pOH.

For a current density of J = 0 mA/cm^2, the pOH equals 7.2 everywhere (pOH of CO_2-saturated 100 mM $KHCO_3$). When the current is non-zero, the local pOH decreases because OH^- is created as a byproduct of CO_2R. The pOH is lower at the electrode surface than 20 µm above the surface because CO_2 is reduced at the electrode surface and for the pOH to decrease at +20 µm, OH^- has to diffuse away from the surface. Due to electrolyte flow, a concentration gradient is created. Furthermore, the pOH inside the trench is lower than at the surface. This can be seen especially well in the panels for current densities of -2 mA/cm^2 and -20 mA/cm^2.

The surface morphology of copper does not change during CO_2R experiments. We performed SEM as well as EDS measurements for samples before and after CO_2R. We observed potassium deposits on the sample after CO_2R that originate from $KHCO_3$ molecules in the electrolyte, but the copper catalyst doesn't change in appearance, neither in the trenches nor on the planar electrode surface (see **Figure S2**).

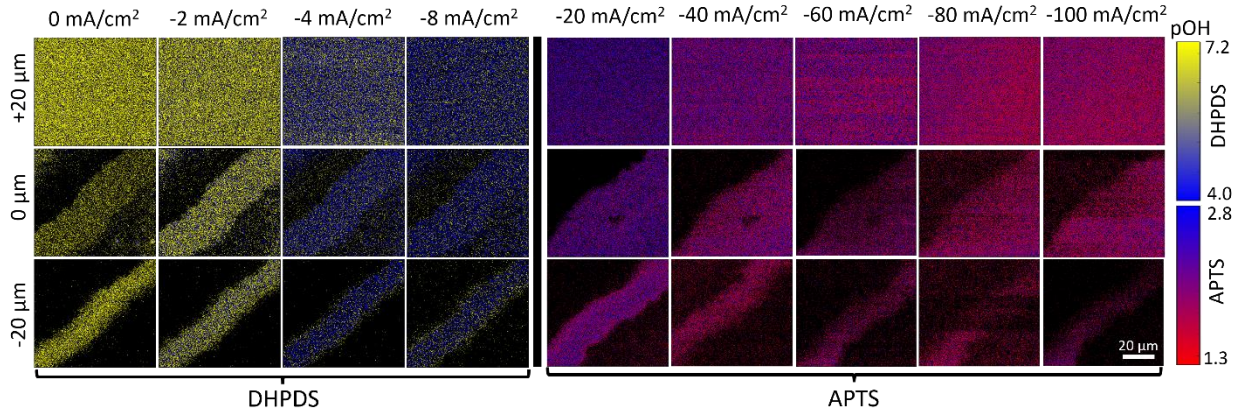

***Figure 3**: pOH maps in the plane parallel to the electrode surface 20 µm above the surface, at the surface and 20 µm below the surface inside a trench in 100 mM $KHCO_3$ electrolyte for different current densities between 0 mA/cm² and -100 mA/cm², obtained with 100 µM DHPDS (left) and 200 µM APTS (right). Note the different color legends for the panels obtained with DHPDS and APTS.*

Figure 4 shows the average pOH as a function of current density, both from experiments and from multiphysics simulations. For the experimental values, the pOH is averaged over at least three independent measurements. The data for low current densities was obtained with DHPDS, while the data for higher current densities was obtained with APTS. The red shaded areas indicate the pOH range that is inaccessible by either dye. The insets are a zoom-in on the experimental data for low current densities.

Simulations were performed to understand better the variations of pOH with respect to position, electrolyte concentration and trench geometry. A 2-dimensional continuum model of a periodic trench in a GDE was developed. The multiphysics simulations solve for the concentration profiles of all species involved, along with the liquid electrolyte potential in a single, periodic trench of a given width and depth. Concentration-dependent Tafel kinetics are employed to simulate the electrochemical reduction of CO_2 to various products on the Cu electrode surface.[35],[36] Greater detail regarding the physics, parameters, and assumptions employed in the continuum model (shown schematically in **Figure S11**) can be found in the Supporting Information, section **S2**. The model replicates the experimental results with outstanding accuracy. This is true both for the pOH values observed in all panels in **Figure 4** as well as for the product distribution that was measured with gas chromatography. The agreement between model and experiment gives us confidence that the model is a good representation of the real world and that predictions that go beyond what can be observed in experiments can be trusted.

Figure 4a compares the pOH in 200 mM $KHCO_3$ electrolyte at positions around a GDE analogous as shown in **Figure 3**. As the current density increases, the pOH decreases accordingly, due to the generation of OH^- from the CO_2R reactions. At first, the slope of the pOH decrease is steep, then gradually tapers as the current density increases. This can be explained by the logarithmic nature of the pOH scale. A decrease in pOH from 4 to 3 requires the OH^- concentration to increase from 0.1 mM to 1 mM, while a decrease in the pOH from 2 to 1 requires the OH^- concentration to rise from 10 mM to 100 mM, a much

larger absolute change in concentration. The pOH in trenches is lower than at the surface, which again is lower than 20 µm above the surface for all current densities; this confirms our previously described results. The simulations agree well with the CLSM experiments, particularly for data at the electrode surface (z = 0 µm) and in the trench (z = −20 µm). Agreement between experiments and simulations is similarly strong for bulk electrolyte concentrations of 100 mM and 400 mM (**Figure S10a-c**). The greatest discrepancy between experiments and simulations is apparent in the z = +20 µm data, which more closely represents the pOH of the bulk electrolyte. The discrepancy is likely due to the static nature of the boundary layer in the simulations, which is set to a constant value of 150 µm, regardless of the applied current density. Previous experimental studies have shown that the bulk electrolyte pH, and thus, the boundary layer thickness is a function of current density at higher current densities.[25],[34] However, implementing an adaptive, 2-D mesh that grows with current would be very computationally intensive, and for the present study, the pOH in the trench, where CO_2R occurs, is more critical to simulate accurately.

Figure 4b displays a study of the influence of $KHCO_3$ concentration in the electrolyte on the pOH at the GDE surface. The trend observed at the electrode surface is the same as it is 20 µm above the electrode surface and 20 µm below in the trenches (**Figure S10d-f**). Measurements for higher concentrations could be carried out at higher current densities due to the enhanced electrical conductivity of the electrolyte. Again, the model generally agrees with observed experimental trends that show that the pOH decreases more slowly as electrolyte concentration is increased. This is because $KHCO_3$ acts as a buffer and, as the $KHCO_3$ concentration increases, the buffering capacity is enhanced, which restrains the decrease in pOH. However, at higher current densities, the simulated pOH becomes more independent of current density whereas the experimental pOH remains impacted by buffer capacity. This discrepancy at higher current densities can be attributed to a multitude of factors, such as the large uncertainty in the rate constants for the homogeneous-phase buffer reactions used in the simulations,[28],[58],[59] and the fact that dilute-solution theory was employed in the simulations whereas concentrated solution theory may be necessary to simulate adequately the behavior at higher current density.[60] Additionally, the simulations assume that there are no mass transport losses of gas phase CO_2 throughout the GDE itself, and thus the CO_2 concentration is at a constant value of 34 mM at the electrode surface. This assumption is likely unrealistic at high current densities and could potentially impact the simulated pOH due to the participation of CO_2 in homogeneous buffer reactions. Nonetheless, the simulations are capable of generally capturing the impact of buffer composition, and the incorporation of these second-order phenomena is beyond the scope of the present study.

Lastly, the influence of the trench geometry on the local pOH was investigated (**Figure 4c**). Eighteen trenches with different widths in 100 mM $KHCO_3$ were taken into consideration. The average pOH inside the trenches, i.e. 20 µm below the surface, was evaluated at different current densities. The trenches were divided into widths of 5 - 10 µm, 10 - 15 µm, 15 - 20 µm, and >20 µm and the average pOH was calculated for each. Both measurements and simulations agree that the pOH decreases as trench width diminishes for all current densities investigated. This behavior is due to the increased surface-area-to-volume-ratio of the thinner trenches (**Figure S13**). The increased surface-area-to-volume ratio means that more OH^- is generated via CO_2R on the trench walls relative the electrolyte volume contained within a trench. In addition, the mass transfer out of trenches is poor compared to a planar surface, which leads to trapping of OH^-. Thus, the OH^- concentration is increased for thinner trenches as a result of both the increased surface-area-to-volume-ratio as well as mass transport effects. This result is in line with previously reported electrochemical studies that have demonstrated that smaller pore radii in meso- or micro-structured electrodes enhance local OH^- trapping.[54],[62],[63] Interestingly, the measured pOH is less

sensitive to trench width at higher current densities than the simulated pOH. A possible explanation for this discrepancy could be the lack of bubble-induced convection in the present simulations. At high current densities, the latter could ameliorate OH^- trapping within GDE trenches and reduce sensitivity to trench geometry. The influence of trench width on the pOH further emphasizes the importance to understand how a GDE's micrometer-scale geometry affects CO_2R.

When we combine the results from **Figure 4 (a)** and **(c)**, we find that the pOH is decreased inside trenches compared to the planar electrode surface and furthermore, this effect is stronger for narrower trenches. This observation is caused by the altered mass transport inside narrow trenches. Our experiments therefore suggest that the micrometer-scale morphology of a gas diffusion electrode plays an important role in determining the mass transport properties of a GDE, and with it the CO_2R performance.

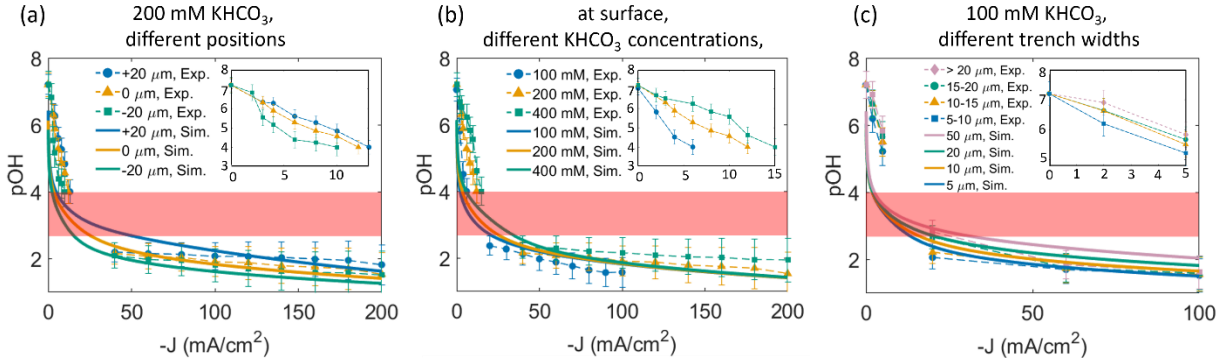

***Figure 4**: The pOH as a function of current density at different positions **(a)**, for different $KHCO_3$ concentrations **(b)** and for different trench widths **(c)**, in experiments and simulations. **(a)** Averaged pOH as a function of current density for 200 mM $KHCO_3$, obtained with 100 µM DHPDS ($J \geq -13$ mA/cm^2)/ 300 µM APTS ($J \leq -20$ mA/cm^2) at three different positions around the electrode surface together with simulation results. **(b)** Averaged pOH as a function of current density at the electrode surface for three different $KHCO_3$ concentrations between 100 and 400 mM, obtained with 100 µM DHPDS ($J \geq -15$ mA/cm^2)/ 200-300 µM APTS ($J \leq -20$ mA/cm^2) together with simulation results. **(c)** pOH inside a trench 20 µm below the surface as a function of current density for different trench widths between 5 µm and 30 µm. In all panels, the pOH range shaded in red is not accessible by either dye, the inset is a zoom on the data for low current densities.*

Beyond elucidating trends observed in the CLSM experiments, continuum simulations can be used to identify pOH variations at resolutions that are not achievable experimentally. **Figure 5a** depicts OH^- transport within a simulated periodic GDE trench operating at a current density of -50 mA/cm^2 (OH^- transport for -1, -10, and -100 mA/cm^2 is depicted in **Figure S15**). As shown in the contour plot, the pOH is lowest, and thus the concentration of OH^- is greatest deep within the trench. Examination of the OH^- flux rationalizes the diminished pOH within the trench: OH^- generated via CO_2R in the trench exits to the bulk electrolyte, but the presence of the trench increases the surface area available for the electrochemical reduction of CO_2 and, accordingly, the generation of OH^-. The trench also provides a volume where the generated OH^- can accumulate due to the altered mass transport. OH^- generated by CO_2R in the trench is thus effectively trapped within the trench, decreasing the local pOH. Similar OH^- trapping behavior has been observed in prior multi-dimensional continuum studies of mesostructured electrodes[38],[58] and has been shown to be beneficial for CO_2R selectivity.[38]

To evaluate the influence of the pOH gradient within the trench on local selectivity variations, concentration-dependent Tafel kinetics were employed in the multiphysics model. These concentration dependent Tafel kinetics were fit to experimental data collected on Cu GDEs used in the present study, and are capable of replicating observed partial current densities quite well (**Figure S12**). The study relates local changes in OH^- activity to changes in current densities for product formation. **Figure 5b** depicts the change in pH as a function of depth into the trench. Note that **Figure 5b** shows the pH value while for the most part, this study focuses on the dynamics of OH^- and hence, the pOH. Here, we chose to display the pH instead to emphasize the correlation between **Figure 5b** and **5c.** In the model, the relation pH + pOH = 14 holds true everywhere because we only consider the diffuse transport layer while the electrical double layer is not taken into consideration in the model because its length scale is much smaller than the length scales we study. Therefore, within the frame of this model, pH and pOH are directly connected. Consistent with **Figure 5a**, pH increases (pOH decreases) deeper inside the trench (more negative *z*) due to trapping of CO_2R-generated OH^-.

The simulations exhibit a direct, albeit modest, relationship between pH and C_{2+} FE (**Figure 5c**). As the pH increases or the pOH decreases within the trench, the C_{2+} FE correspondingly increases (variations of C_1, H_2, and local current density within the trench are shown in **Figure S15**). This relationship between C_{2+} FE and pH has been widely reported, and is connected to the suppression of HER and C_1 products.[9],[19],[35],[36],[63] The disproportionate suppression of H_2, CH_4, and HCOOH partial current density within the trench can be observed in **Figure S16.** This suppression of C_1 and H_2 in the trench results in an approximately 5% increase in C_{2+} FE across the depth of the trench, regardless of current density (**Figure 5c**). The enhancement of the performance in the trench is modest, as the change in pH is only about 1 pH unit across the trench depth. Nonetheless, the simulations serve to understand local selectivity trends and provide better understanding of variations in performance within the GDE heterogeneities.

Lastly, performance of CO_2R within trenches was compared to the performance on a flat surface without trenches (**Figure 5d**). The simulations demonstrate that the C_{2+} FE at a given current density is higher within a trench compared to that on a flat surface due to the improved OH^- trapping. In addition, as the width of the trench decreases, and with it the pOH **(Figure 4c and Figure S18)**, the C_{2+} FE increases. This is a result of the changed mass transport properties in the confined space as well as the enhanced trench surface-area-to-volume ratio (**Figure S13**), leading to a lower pOH value. The simulations indicate that the micrometer-scale morphology on a GDE surface has an impact on the product distribution with narrow trenches on the order of 5 µm favoring the creation of C_{2+} products across the entire current density range **(Figure 5d**) by approximately 5% compared to the flat Cu case. Within the scope of this work, the connection between surface morphology and CO_2R selectivity can only be demonstrated via multiphysics simulations because we have no means to locally resolve the product distribution. However, the accuracy of our model has been demonstrated as there is an excellent agreement with the experimentally measured CO_2R performance as well as the local pOH. Nonetheless, the simulations demonstrate the potential for improved C_{2+} FE within these microcavities and experimental demonstration of enhanced C_{2+} FE inside microcavities in the surface of an operating GDE should be the subject of a future study.

The effect of the trench depth on CO_2R was also evaluated (**Figure S19**), which demonstrates that the ability of a trench to enhance C_{2+} FE increases as the trench deepens. This is due to the increased surface area available for electrochemical OH^- generation for deeper trenches. The surface-area-to-volume ratio is far less sensitive to trench depth than to trench width (**Figure S18**) which indicates that compared to the surface area, the volume plays a minor role in determining the C_{2+} FE. However,

enhancements in C_{2+} FE become marginal beyond trench depths of 50 µm. Finally, the fraction of the surface covered by the trenches was varied in the simulations, to further evaluate the efficacy of trenches. **Figure S20** depicts the pOH and C_{2+} FE as a function of trench coverage, evaluated at current densities of -20 mA/cm^2 and -50 mA/cm^2 (normalized now to the electrochemical active surface area (ECSA)). This figure aims to deconvolute the effects of roughness from the effects of changes in the microenvironment. As the trench surface coverage increases, the pOH decreases, and the C_{2+} FE increases, due to the OH^- trapping ability of the trenches. While the increase in C_{2+} FE is minor (still approximately 5 % from a flat surface to a completely trenched surface), the enhancement with morphology is similarly observed at both current densities and the results reveal that heterogeneities in commercially available GDEs can serve as local hotspots for enhanced C_{2+} FE and benefit CO_2R due to their OH^- trapping capacity. The simulation results serve as a great support to our novel measurements that allow to probe the microenvironment in a GDE under operando conditions. Both experiment and simulations highlight the importance of the micromorphology of a GDE that influences the mass transport properties. Future work should aim to leverage this insight to develop geometries for which transport is tailored to better trap OH^-. Techniques like laser ablation can be utilized to realize these tailored electrodes.

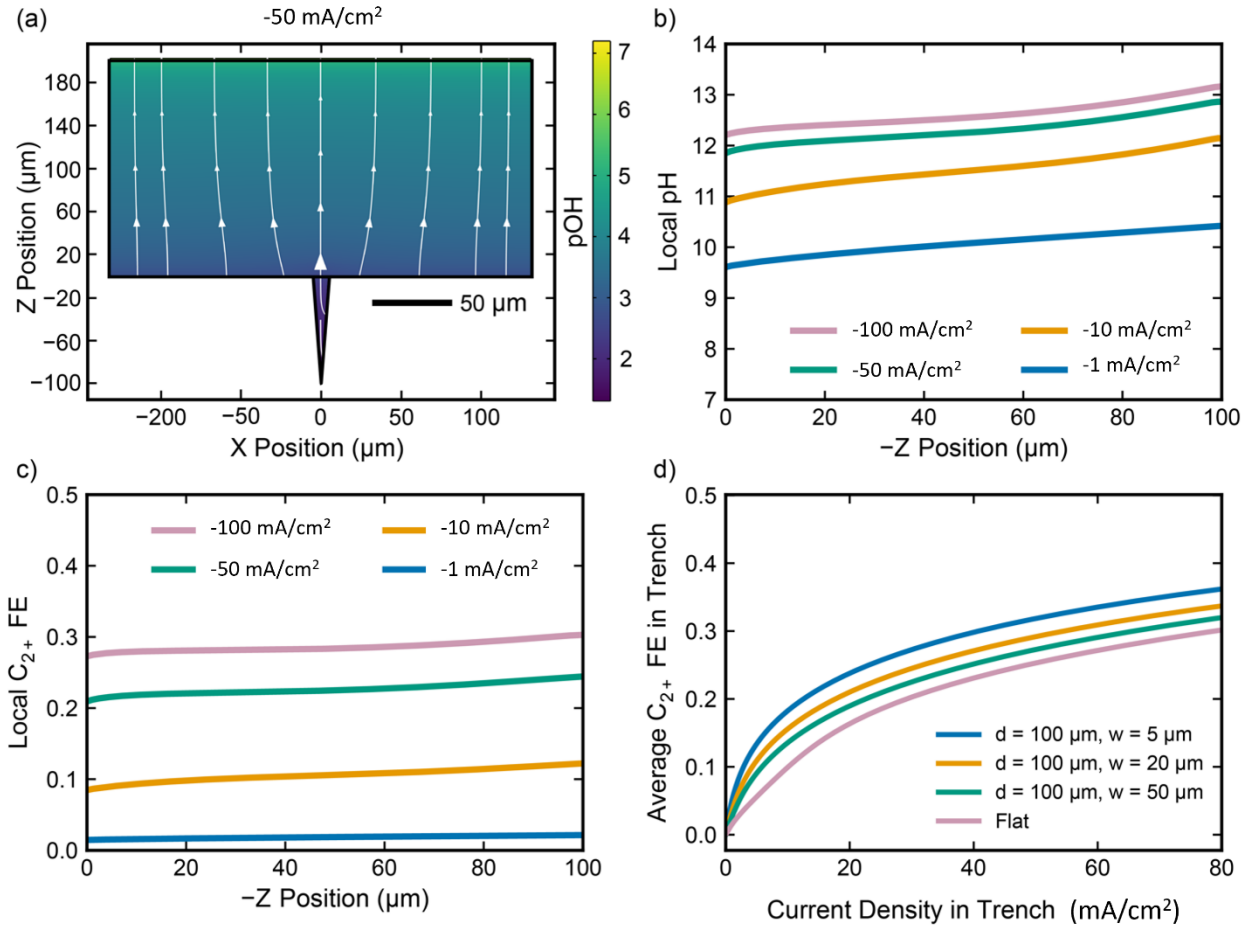

***Figure 5**: **(a)** pOH contour plot and OH^- flux (white arrows) throughout the simulated domain for a periodic GDE trench (width of 20 µm and depth of -100 µm) operating at -50 mA/cm^2 of geometric current density (see section **S4** for a description of how geometric current density is calculated). **(b)** Simulated electrode surface pH (14 – pOH) as a function of depth into the trench for different current densities. **(c)** Simulated*

C_{2+} FE as a function of depth into the trench for different current densities. ***(d)*** *Average C_{2+} FE on trench walls as a function of the current density passed solely through the trench. Z = 0 µm represents the top of the trench, and Z = −100 µm represents the bottom of the trench. d and w are the trench depth and width, respectively.*

Conclusions

We demonstrate a novel technique to probe the microenvironment in a CO_2R GDE under operating conditions. We map the local pOH value around a GDE resolved in time and three spatial dimensions with fluorescent confocal laser scanning microscopy (CLSM) with a combination of two ratiometric dyes, DHPDS and APTS, that operate by different sensing mechanisms. The novel application of APTS as a dynamic excited-state pOH probe was demonstrated for the first time. Critically, this work could hold potential applications beyond the investigation of CO_2R. We were able to capture pOH maps in the pOH range between 0 and 8 and at current densities as large in magnitude as -200 mA/cm^2.

In a first step, we investigated the diffusion patterns of CO_2 through a GDE. This study revealed that CO_2 diffuses through microcavities first, and that electrolyte flow leads to a CO_2 concentration gradient with the highest concentration confined to trenches. These microcavities in a GDE surface as well as large pore sizes promote faster CO_2 transport, highlighting the importance to understand the influence of the micron-scale morphology of a CO_2R GDE.

We mapped the local pOH around an operating GDE under applied current. This revealed that the pOH in the vicinity of a GDE decreases as current density is increased. For all current densities covered, the pOH inside trenches is lower than on the planar surface with the lowest pOH observed inside narrow trenches that are approximately 5 µm wide. This decrease in pOH can be connected to the trapping of OH^- in narrow trenches caused by altered mass transport properties.

Multiphysics simulations confirmed all experimental trends, providing pOH maps consistent with measured pOH and also reproduced product distributions with high accuracy. These simulations indicate that there is a correlation between the pOH and the Faradaic efficiency towards C_{2+} products. Narrow trenches exhibit a decreased pOH and simulations suggest that this results in a locally increased Faradaic efficiency towards C_{2+} products.

We conclude that we successfully developed a superior technique to probe the microenvironment around a CO_2R GDE. The micrometer-scale morphology of a GDE has a strong effect on the mass transport properties and with it, on the CO_2R performance. Microcavities on the order of 5 µm on the surface of a copper GDE serve as local hotspots with decreased pOH. We expect that this will inform the design of future CO_2R devices.

Author Contributions

AB performed dye calibration and all pOH imaging experiments as well as data analysis and wrote the original draft of the manuscript. JCB and AJK developed the multiphysics model with oversight by AZW. JCB ran simulations and performed data analysis on results from the multiphysics model. AF conducted the gas chromatography measurements. RB contributed to conceptualization of the choice of APTS photoacid. CNF investigated possible interference in signal from APTS due to dissolved inorganic carbon

species. AJW developed the experimental setup and designed the electrochemical cell. AB, AF, RB, AJW, SA and HAA contributed to the conceptualization of the study. JCB, AF, RB, AJW, ATB, AZW, SA and HAA reviewed and edited the manuscript. ATB, AZW, SA and HAA supervised the project. All authors discussed the results and contributed to the preparation of the manuscript.

Conflicts of Interest

There are no conflicts to declare.

Acknowledgements

This material is based on work performed within the Liquid Sunlight Alliance, which is supported by the U.S. Department of Energy, Office of Science, Office of Basic Energy Sciences, Fuels from Sunlight Hub under Award Number DE-SC0021266. JCB would like to acknowledge support from the National Defense Science and Engineering Graduate Fellowship (NDSEG) supported by the Army Research Office (ARO). The authors thank Ian Sullivan for 3D-printing the electrochemical cell.

References

(1) S. Jin, Z. Hao, K. Zhang, Z. Yan, J. Chen, Advances and Challenges for the Electrochemical Reduction of CO_2 to CO: From Fundamentals to Industrialization. *Angew. Chem.,* 2021, **133**, 2–24.

(2) S. J. Davis, N. S. Lewis, M. Shaner, S. Aggarwal, D. Arent, I. L. Azevedo, S. M. Benson, T. Bradley, J. Brouwer, Y. Chiang, et al. Net-Zero Emissions Energy Systems. *Science* 2018, **360**, 6396.

(3) M.-Y. Lee, K. T. Park, W. Lee, H. Lim, Y. Kwon, S. Kang, Current achievements and the future direction of electrochemical CO_2 reduction: A short review. *Crit Rev Environ Sci Technol* 2020, **50**, 769-815.

(4) J.-P. Jones, G. K. S. Prakash, G. A. Olah, Electrochemical CO_2 Reduction: Recent Advances and Current Trends. *Isr. J. Chem.* 2014, **54**, 1451-1466.

(5) S. Wang, T. Kou, S. E. Baker, E. B. Duoss, Y. Li, Electrochemical Reduction of CO_2 to Alcohols: Current Understanding, Progress, and Challenges. *Adv. Energy Sustainability Res.* 2022, **3**, 2100131.

(6) D. Higgins, C. Hahn, X. Chengxiang, T. F. Jaramillo, A. Z. Weber, Gas-Diffusion Electrodes for Carbon Dioxide Reduction: A New Paradigm. *ACS Energy Lett.* 2019, **4**, 317−324.

(7) M. Inaba, A. W. Jensen, G. W. Sievers, M. Escudero-Escribano, A. Zana, M. Arenz, Benchmarking High Surface Area Electrocatalysts in a Gas Diffusion Electrode: Measurement of Oxygen Reduction Activities under Realistic Conditions. *Energy Environ. Sci.* 2018, **11**, 988−994.

(8) C. Dinh, T. Burdyny, G. Kibria, A. Seifitokaldani, C. M. Gabardo, F. P. G. De Arquer, A. Kiani, J. P. Edwards, P. De Luna, O. S. Bushuyev, et al. CO_2 Electroreduction to Ethylene via Hydroxide-Mediated Copper Catalysis at an Abrupt Interface. *Science* 2018, **360**, 783−787.

(9) B. Kim, F. Hillman, M. Ariyoshi, S. Fujikawa, P. J. A. Kenis, Effects of Composition of the Microporous Layer and the Substrate on Performance in the Electrochemical Reduction of CO_2 to CO. *J. Power Sources* 2016, **312**, 192−198.

(10) L.-C. Weng, A. T. Bell, A. Z. Weber, Modeling Gas-Diffusion Electrodes for CO_2 Reduction. *Phys. Chem. Chem. Phys.* 2018, **20**, 16973−16984.
(11) T. N. Nguyen, C. T. Dinh, Gas Diffusion Electrode Design for Electrochemical Carbon Dioxide Reduction. *Chem. Soc. Rev*. 2020, **49**, 7488−7504.
(12) A. Q. Fenwick, A. J. Welch, X. Li, I. Sullivan, J. S. DuChene, C. Xiang, H. A. Atwater, Probing the Catalytically Active Region in a Nanoporous Gold Gas Diffusion Electrode for Highly Selective Carbon Dioxide Reduction. *ACS Energy Lett.* 2022, **7**, 2, 871-879.
(13) M. R. Singh, E. L. Clark, A. T. Bell, Effects of Electrolyte, Catalyst, and Membrane Composition and Operating Conditions on the Performance of Solar-Driven Electrochemical Reduction of Carbon Dioxide. *Phys. Chem. Chem. Phys.* 2015, **17**, 18924−18936.
(14) F. P. García de Arquer, C. T. Dinh, A. Ozden, J. Wicks, C. McCallum, A. R. Kirmani, D. H. Nam, C. Gabardo, A. Seifitokaldani, X. Wang, X.; et al. CO_2 Electrolysis to Multicarbon Products at Activities Greater than 1 A cm^{-2}. *Science* 2020, **367**, 661−666.
(15) Y. Hori, K. Kikuchi, S. Suzuki, Production of CO and CH_4 in the Electrochemical Reduction of CO_2 at Metal Electrodes in Aqueous Hydrogencarbonate Solution. *Chem. Lett.* 1985, **14**, 1695−1698.
(16) R. Kortlever, J. Shen, K. J. P. Schouten, F. Calle-Vallejo, M. T. M. Koper, Catalysts and Reaction Pathways for the Electrochemical Reduction of Carbon Dioxide. *J. Phys. Chem. Lett.* 2015, **6**, 4073−4082.
(17) A. Bagger, W. Ju, A. S. Varela, P. Strasser, J. Rossmeisl, Electrochemical CO_2 Reduction: A Classification Problem. *Chem. Phys. Chem.* 2017, **18**, 3266−3273.
(18) K. Kuhl, E. R. Cave, D. N. Abram, T. F. Jaramillo, New Insights into the Electrochemical Reduction of Carbon Dioxide on Metallic Copper Surfaces. *Energy Environ. Sci.* 2012, **5**, 7050−7059.
(19) S. Nitopi, E. Bertheussen, S. B. Scott, X. Liu, A. K. Engstfeld, S. Horch, B. Seger, I. E. L. Stephens, K. Chan, C. Hahn, et al. Progress and Perspectives of Electrochemical CO_2 Reduction on Copper in Aqueous Electrolyte. *Chem. Rev.* 2019, **119**, 7610−7672.
(20) P. Jeanty, C. Scherer, E. Magori, K. Wiesner-Fleischer, O. Hinrichsen, M. Fleischer, Upscaling and Continuous Operation of Electrochemical CO_2 to CO Conversion in Aqueous Solutions on Silver Gas Diffusion Electrodes. *J. CO2 Util.* 2018, **24**, 454−462.
(21) E. R. Cofell, U. O. Nwabara, S. S. Bhargava, D. E. Henckel, P. J. A. Kenis, Investigation of Electrolyte-Dependent Carbonate Formation on Gas Diffusion Electrodes for CO_2 Electrolysis. *ACS Appl. Mater. Interfaces* 2021, **13**, 15132 – 15142.
(22) M. R. Singh, Y. Kwon, Y. Lum, J. W. Ager, A. T. Bell, Hydrolysis of Electrolyte Cations Enhances the Electrochemical Reduction of CO_2 over Ag and Cu. *J. Am. Chem. Soc.* 2016, **138**, 13006−13012.
(23) D. M. Weekes, D. A. Salvatore, A. Reyes, A. Huang, C. P. Berlinguette, Electrolytic CO_2 Reduction in a Flow Cell. *Acc. Chem. Res.* 2018, **51**, 910−918.
(24) Y. Y. Birdja, E. Pérez-Gallent, M. C. Figueiredo, A. J. Göttle, F. Calle-Vallejo, M. T. M. Koper, Advances and Challenges in Understanding the Electrocatalytic Conversion of Carbon Dioxide to Fuels. *Nat. Energy* 2019, **4**, 732−745.
(25) Z. Zhang, L. Melo, R. P. Jansonius, F. Habibzadeh, E. R. Grant, C. P. Berlinguette, pH Matters When Reducing CO_2 in an Electrochemical Flow Cell. *ACS Energy Lett.* 2020, **5**, 3101−3107.
(26) D. Kolb, The pH Concept. *J. Chem. Educ.* 1979, **56**, 49-53.
(27) J. A. Rabinowitz, M. W. Kanan, The Future of Low-Temperature Carbon Dioxide Electrolysis Depends on Solving One Basic Problem. *Nat. Commun.* 2020, **11**, No. 5231.

(28) K. G. Schulz, U. Riebesell, B. Rost, S. Thoms, R. E. Zeebe, Determination of the Rate Constants for the Carbon Dioxide to Bicarbonate Inter-Conversion in pH-Buffered Seawater Systems. *Mar. Geochem.* 2006, **100**, 53−65.

(29) G. A. Mills, H. C. Urey, The Kinetics of Isotropic Exchange between Carbon Dioxide, Bicarbonate Ion, Carbonate Ion and Water. *J. Am. Chem. Soc.* 1940, **62**, 1019-1026.

(30) A. J. Garza, A. T. Bell, M. Head-Gordon, Mechanism of CO_2 Reduction at Copper Surfaces: Pathways to C_2 Products. *ACS Catal.* 2018, **8**, 1490-1499.

(31) X. Zhao, L. Du, Y. Sun, Integrated Design for electrocatalytic carbon dioxide reduction. *Catal. Sci. Technol.* 2020, **10**, 2711-2720.

(32) X. Liu, P. Schlexer, J. Xiao, Y. Ji, L. Wang, R. B. Sandberg, M. Tang, K. S. Brown, H. Peng, S. Ringe, C. Hahn, T. F. Jaramillo, J. K. Nørskov, K. Chan, pH Effects on the Electrochemical Reduction of $CO_{(2)}$ towards C_2 Products on Stepped Copper. *Nat. Commun.* 2019, **10**, 32.

(33) J. A. Gauthier, Z. Lin, M. Head-Gordon, A. T. Bell, Pathways for the Formation of C_{2+} Products under Alkaline Conditions during the Electrochemical Reduction of CO_2. *ACS Energy Lett.* 2022, **5**, 1679-1686.

(34) K. Yang, R. Kas, W. A. Smith, In Situ Infrared Spectroscopy Reveals Persistent Alkalinity near Electrode Surfaces during CO_2 Electroreduction. *J. Am. Chem. Soc.* 2019, **141**, 15891−15900.

(35) L. Wang, S. A. Nitopi, E. Bertheussen, M. Orazov, C. G. Morales- Guio, X. Liu, D. C. Higgins, K. Chan, J. K. Nørskov, C. Hahn, T. F. Jaramillo, Electrochemical Carbon Monoxide Reduction on Polycrystalline Copper: Effects of Potential, Pressure, and pH on Selectivity toward Multicarbon and Oxygenated Products. *ACS Catal.* 2018, **8**, 7445−7454.

(36) J. C. Bui, C. Kim, A. Z. Weber, A. T. Bell, Dynamic Boundary Layer Simulation of Pulsed CO_2 Electrolysis on a Copper Catalyst. *ACS Energy Lett.* 2021, **6**, 1181–1188.

(37) N. Nesbitt, W. Smith, Water Activity Regulates CO_2 Reduction in Gas-Diffusion Electrodes. *J. Phys. Chem. C.* 2021, **125**, 24, 13085-13095.

(38) S. Suter, S. Haussener, Optimizing Mesostructured Silver Catalysts for Selective Carbon Dioxide Conversion into Fuels. *Energy Environ. Sci.* 2019, **12**, 1668−1678.

(39) A. Botz, J. Clausmeyer, D. Öhl, T. Tarnev, D. Franzen, T. Turek, W. Schuhmann, Local Activities of Hydroxide and Water Determine the Operation of Silver-Based Oxygen Depolarized Cathodes. *Angew. Chem., Int. Ed.* 2018, **57**, 12285−12289.

(40) S. Dieckhöfer, D. Öhl, J. R. C. Junqueira, T. Quast, T. Turek, W. Schuhmann, Probing the Local Reaction Environment During High Turnover Carbon Dioxide Reduction with Ag-Based Gas Diffusion Electrodes. *Chem. - Eur. J.* 2021, **27**, 5906−5912.

(41) X. Lu, C. Zhu, Z. Wu, J. Xuan, J. S. Francisco, H. Wang, In Situ Observation of the pH Gradient near the Gas Diffusion Electrode of CO_2 Reduction in Alkaline Electrolyte. *J. Am. Chem. Soc.* 2020, **142**, 15438−15444.

(42) N. Nesbitt, W. A. Smith, Operando Topography and Mechanical Property Mapping of CO_2 Reduction Gas-Diffusion Electrodes Operating at High Current Densities. *J. Electrochem. Soc.* 2021, **168**, No. 044505.

(43) M. C. O. Monteiro, M. T. M. Koper, Measuring Local pH in Electrochemistry. *Curr. Opin. Electrochem.* 2021, **25**, No. 100649.

(44) N. C. Rudd, S. Cannan, E. Bitziou, I. Ciani, A. Whitworth, P. R. Unwin, Fluorescence Confocal Laser Scanning Microscopy as a Probe of pH Gradients in Electrode Reactions and Surface Activity. *Anal. Chem.* 2005, **77**, 6205−6217.

(45) L. Bouffier, T. Doneux, Coupling Electrochemistry with In Situ Fluorescence (Confocal) Microscopy. *Curr. Opin. Electrochem.* 2017, **6**, 31−37.
(46) N. Pande, S. K. Chandrasekar, D. Lohse, G. Mul, J. A. Wood, B. T. Mei, D. Krug, Electrochemically Induced pH Change: Time-Resolved Confocal Fluorescence Microscopy Measurements and Comparison with Numerical Model. *J. Phys. Chem. Lett.* 2020, **11**, 7042−7048.
(47) J. E. Vitt, R. C. Engstrom, Imaging of Oxygen Evolution and Oxide Formation Using Quinine Fluorescence. *Anal. Chem.* 1997, **69**, 1070−1076.
(48) W. J. Bowyer, J. Xie, R. C. Engstrom, Fluorescence Imaging of the Heterogeneous Reduction of Oxygen. *Anal. Chem.* 1996, **68**, 2005−2009.
(49) A. J. Welch, A. Q. Fenwick, A. Boehme, H.-Y. Chen, I. Sullivan, X. Li, J. DuChene, C. Xiang, H. A. Atwater, Operando Local pH Measurement within Gas Diffusion Electrodes Performing Electrochemical Carbon Dioxide Reduction. *J. Phys. Chem. C.* 2021, **125**, 20896-20904.
(50) R. Gui, H. Jin, X. Bu, Y. Fu, Z. Wang, Q. Liu, Recent advances in dual-emission ratiometric fluorescent probes for chemo/biosensing and bioimaging of biomarkers. *Coord. Chem. Rev.* 2019, **383**, 82-103.
(51) M. H. Lee, J. S. Kim, J. L. Sessler, Small molecule-based ratiometric fluorescent probes for cations, anions, and biomolecules. *Chem. Soc. Rev.* 2015, **44**, 4185.
(52) S.-H. Park, N. Kwon, J.-H. Lee, J. Yoon, I. Shin, Synthetic ratiometric fluorescent probes for detection of ions. *Chem. Soc. Rev.* 2020, **49**, 143-179.
(53) A. Hakonen, S. A. Hulth, High-Performance Fluorosensor for pH Measurements between 6 and 9. *Talanta* 2010, **80**, 1964−1969.
(54)J. M. Spurgeon, B. Kumar, A comparative technoeconomic analysis of pathways for commercial electrochemical CO_2 reduction to liquid products. *Energy Environ. Sci.* 2018, **11**, 1536.
(55) M. G. Kibria, J. P. Edwards, C. M. Gabardo, C.-T. Dinh, A. Seifitokaldani, D. Sinton, E. H. Sargent, Electrochemical CO_2 Reduction into Chemical Feedstocks: From Mechanistic Electrocatalysis Models to System Design. *Adv. Mater.* 2019, **31**, 1807166.
(56) R. Bhide, C. N. Feltenberger, G. S. Phun, G. Barton, D. Fishman, S. Ardo, Quantification of Excited-State Brønsted-Lowry Acidity of Weak Photoacids Using Steady-State Photoluminescence Spectroscopy and a Driving-Force-Dependent Kinetic Theory. *J. Am. Chem. Soc.* 2022, in press, DOI: 10.1021/jacs.2c00554.
(57) M. Sassenburg, R. de Rooji, N. T. Nessbitt, R. Kas, S. Chandrashekar, N. J. Firet, K. Yang, K. Liu, M. A. Blommaert, M. Kolen, D. Ripepi, W. A. Smith, T. Burdyny, Characterizing CO2 Reduction Catalysts on Gas Diffusion Electrodes: Comparing Activity, Selectivity and Stability of Transition Metal Catalysts. *ACS Appl. Energy Mater.* **2022**, 5, 5983-5994.
(58) J. C. Bui, E. W. Lees, L. M. Pant, I. V. Zenyuk, A. T. Bell, A. Z. Weber, Continuum Modeling of Porous Electrodes for Electrochemical Synthesis. *Chem. Rev.* 2022, **122**, 12, 11022-11084.
(59) M. Eigen, Proton Transfer, Acid-Base Catalysis, and Enzymatic Hydrolysis. *Angew. Chemie* 1964, **3** (I), 1–19.
(60) V. M. Ehlinger, A. R. Crothers, A. Kusoglu, A. Z. Weber, Modeling Proton-Exchange-Membrane Fuel Cell Performance/ Degradation Tradeoffs with Chemical Scavengers. *J. Phys. Energy* 2020, **2** (4), 044006.
(61) A. S. Hall, Y. Yoon, A. Wuttig, Y. Surendranath, Mesostructure-Induced Selectivity in CO_2 Reduction Catalysis. *J. Am. Chem. Soc.* 2015, **137**, 14834−14837.

(62) A. J. Welch, J. S. Duchene, G. Tagliabue, A. Davoyan, W. H. Cheng, H. A. Atwater, Nanoporous Gold as a Highly Selective and Active Carbon Dioxide Reduction Catalyst. *ACS Appl. Energy Mater.* 2019, **2**, 164−170.

(63) C. Kim, J. C. Bui, X. Luo, J. K. Cooper, A. Kusoglu, A. Z. Weber, A. T. Bell, Tailored Catalyst Microenvironments for CO_2 Electroreduction to Multicarbon Products on Copper Using Bilayer Ionomer Coatings. *Nat. Energy* 2021, **6** (11), 1026–1034.

(64) C. Kim, L. C. Weng, A. T. Bell, Impact of Pulsed Electrochemical Reduction of CO_2 on the Formation of C_{2+} Products over Cu. *ACS Catal.* 2020, **10** (21), 12403–12413.

(65) S. Ringe, E. L. Clark, J. Resasco, A. Walton, B. Seger, A.-T. Bell, K. Chan, Understanding Cation Effects in Electrochemical CO_2 Reduction. *Energy Environ. Sci.* 2019, **12** (10), 3001–3014.

(66) J. Resasco, L. D. Chen, E. Clark, C. Tsai, C. Hahn, T. F. Jaramillo, K. Chan, A. T. Bell, Promoter Effects of Alkali Metal Cations on the Electrochemical Reduction of Carbon Dioxide. *J. Am. Chem. Soc.* 2017, **139** (32), 11277–11287.

(67) B. A. Pinaud, J. D. Benck, L. C. Seitz, A. J. Forman, Z. Chen, T. G. Deutsch, B. D. James, K. N. Baum, G. N. Baum, S. Ardo, H. Wang, E. Miller, T. F. Jaramillo, Tenchnical and economic feasibility of centralized facilities for solar hydrogen production via photocatalysis and photoelectrochemistry. *Energy Environ. Sci.* 2013, **6**, 1983-2002.

(68) I. Roh, S. Yu, C.-K. Lin, S. Louisia, S. Cestellos-Blanco, P. Yang, Photoelectrochemical CO_2 Reduction toward Multicarbon Products with Silicon Nanowire Photocathodes Interfaced with Copper Nanoparticles. *J. Am. Chem. Soc.* 2022, **144**, 18, 8002-8006.

(69) C. Corral, J. T. Reaster, S. Sobhani, J. R. DeOtte, D. Un Lee, A. W. Wong, J. Hamilton, V. A. Beck, A. Sarkar, C. Hahn, T. F. Jaramillo, S. E. Baker, E. B. Duoss, Advanced manufacturing for electrosynthesis of fuels and chemicals from CO_2. *Energy Environ. Sci.* 2021, **14**, 3064.